論文 / 著書情報
Article / Book Information

Title	Modelling geomagnetic induction hazards using a 3-D electrical conductivity model of Australia
Authors	Wang L., Lewis A., Ogawa Y, Jones W., Costelloe M.
Citation	Space Weather, Vol. 14, ,
Pub. date	2016, 10
Copyright	Copyright (c) 2016 American Geophysical Union (AGU)
Creative Commons	The information is in the article.

License

AGU PUBLICATIONS

Space Weather

RESEARCH ARTICLE
10.1002/2016SW001436

Key Points:
- The induced electric fields at the surface are modeled using a 3-D electrical conductivity model of Australia
- Geophysical and geological interpretations are applied to the distortions in the induced electric fields
- GIC estimates in Australia are assessed for effects of 3-D Earth conductivity

Correspondence to:
L. Wang,
liejun.wang@ga.gov.au

Citation:
Wang, L., A. M. Lewis, Y. Ogawa, W. V. Jones, and M. T. Costelloe (2016), Modeling geomagnetic induction hazards using a 3-D electrical conductivity model of Australia, *Space Weather*, *14*, doi:10.1002/2016SW001436.

Received 30 MAY 2016
Accepted 5 OCT 2016
Accepted article online 7 OCT 2016

Modeling geomagnetic induction hazards using a 3-D electrical conductivity model of Australia

Liejun Wang[1], Andrew M. Lewis[1], Yasuo Ogawa[2], William V. Jones[1], and Marina T. Costelloe[1]

[1]Geoscience Australia, Canberra, ACT, Australia, [2]Volcanic Fluid Research Center, Tokyo Institute of Technology, Tokyo, Japan

Abstract The surface electric field induced by external geomagnetic source fields is modeled for a continental-scale 3-D electrical conductivity model of Australia at periods of a few minutes to a few hours. The amplitude and orientation of the induced electric field at periods of 360 s and 1800 s are presented and compared to those derived from a simplified ocean-continent (OC) electrical conductivity model. It is found that the induced electric field in the Australian region is distorted by the heterogeneous continental electrical conductivity structures and surrounding oceans. On the northern coastlines, the induced electric field is decreased relative to the simple OC model due to a reduced conductivity contrast between the seas and the enhanced conductivity structures inland. In central Australia, the induced electric field is less distorted with respect to the OC model as the location is remote from the oceans, but inland crustal high-conductivity anomalies are the major source of distortion of the induced electric field. In the west of the continent, the lower conductivity of the Western Australia Craton increases the conductivity contrast between the deeper oceans and land and significantly enhances the induced electric field. Generally, the induced electric field in southern Australia, south of latitude −20°, is higher compared to northern Australia. This paper provides a regional indicator of geomagnetic induction hazards across Australia.

1. Introduction

A magnetic storm is a geomagnetic disturbance, often with a storm sudden commencement or sudden impulse, followed by a day or two of growth and evolution then a gradual return to a state of relative quiescence [*Love and Swidinsky*, 2015]. The fundamental principle for induction hazards is that time-varying geomagnetic fields caused by geomagnetic storms and other natural field variations induce electric fields in the Earth's surface and interior. The induced electric field then drives uncontrolled geomagnetically induced currents (GICs) in the ground which themselves have an associated secondary magnetic field.

Australia is situated at middle to low latitudes under the path of the solar quiet (Sq) focus [*Campbell and Schiffmacher*, 1988]. Magnetospheric and ionospheric current systems such as the magnetopause current, ring current, and equatorial electrojet are possible sources for GIC hazards [*Marshall et al*., 2012].

The potential hazards posed by magnetic storms and associated GICs for long-distance conductive ground infrastructure such as power networks [*Boteler et al*., 1998; *Marshall et al*., 2011, 2012] and pipelines [*Fernberg et al*., 2007; *Marshall et al*., 2010] are well documented. A GIC index representing the GIC activity level in the Australian region has been defined by *Marshall et al*. [2011]. The index is derived from magnetic time series data by utilizing a frequency domain filter based on a 1-D conductivity structure model. The GIC index thresholds in Australia for low and moderate risk are 50 and 100, respectively. *Marshall et al*. [2010, 2011] have shown that the risk of GIC to technical networks could have reached moderate levels a few times in southern Australian regions and 20 times in the southernmost Australian state of Tasmania during solar cycle 23 (from 1997 to 2008).

Barton [1997] developed a continent-scale "aeromagnetic risk factor map" representing the risk posed by geomagnetic induction hazards to aeromagnetic surveys. The risk factor was derived from the variability of the length and direction of induction arrows (defined in equation (4) in section 2) [*Parkinson*, 1962] obtained from the Australia Wide Array of Geomagnetic Stations (AWAGS) data [*Chamalaun and Barton*, 1990] for periods of 42 to 80 min. The aeromagnetic risk factor risk map clearly reflects the inductive influence of oceans and continental electrical conductivity anomalies. With the availability of a 2.5-D thin-sheet model for the continent [*Wang and Lilley*, 1999], *Lilley et al*. [1999] modeled the continent-scale geomagnetic induction hazard for total-field magnetic surveys at a single period of 60 min. The geomagnetic induction due to 3-D

Earth conductivity poses a risk to the removal of temporal magnetic variations from total magnetic field survey data [*Barton*, 1997; *Lilley et al*., 1999], just as it poses a risk to the accuracy of GIC estimates which are addressed by this study.

Bedrosian and Love [2015] used empirical impedance tensors derived directly from the USArray magnetotelluric measurements in the United States and a synthetic north-south geomagnetic sinusoidal source field with a period of 100 s and amplitude 1 nT to calculate electric field variations. The synthetic results at a period of 300 s demonstrated that the calculated electric field vectors could differ by a factor of 100 in amplitude and up to 130° in direction due to effects of 3-D Earth conductivity structures. Their approach has advanced the calculation of GIC estimates over those calculated from simple 1-D depth-dependent electrical conductivity models.

Advances in electrical conductivity models of Australia from a 2.5-D thin-sheet [*Wang and Lilley*, 1999] to a 3-D model [*Wang et al*., 2014] make it now possible to model the induced electric field distributions over a wider frequency range relevant to GIC studies. The modeling provides insight into potential geomagnetic induction hazards across Australia due to oceans and 3-D conductivity structures from the surface to a depth of over 600 km. This paper investigates how 3-D electrical conductivity structures affect GIC predications in Australia.

2. Modeling the Induced Electric Field With a 3-D Model

2.1. Description of Modeling Method

The modeling of GIC in technological networks is usually divided into two independent steps: the geophysical step and the engineering step. The geophysical step involves the calculation of the induced electric field based on knowledge of the ionospheric and magnetospheric source currents and the ground conductivity structure. The engineering step is the calculation of the GIC based on knowledge of the induced electric field and the topology and electrical parameters of a technological network [*Pulkkinen*, 2003; *Zhang et al*., 2015] and is beyond the scope of this paper.

In the geophysical step the induced electric field that drives the GIC is often derived with the assumption of plane wave geomagnetic source fields and a homogeneous or layered conductivity structure [*Love and Swidinsky*, 2015]. Under the plane wave source assumption, the horizontal electric field (E_x, E_y) in mV/km and the magnetic induction field (B_x, B_y) in nT have a frequency-dependent linear relationship via magnetotelluric (MT) tensors (M) following the notation of *Weaver et al*. [2000]:

$$\begin{aligned} E_x &= M_{xx}B_x + M_{xy}B_y \\ E_y &= M_{yx}B_x + M_{yy}B_y \end{aligned} \tag{1}$$

The MT tensors (M) are in units of mV/km nT. The relation to impedance tensors (Z) in Ohms is $Z = \mu_0 M$ where μ_0 is the magnetic permeability of free space. The x and y components are the geographic north and east components of the electromagnetic fields in Cartesian coordinates.

The MT tensors are cast in the form of telluric vectors (e_x, e_y) representing the electric field induced by a normalized 1 nT magnetic field linearly polarized in a northerly mode (field polarization azimuth $\theta = 0°$) and an easterly mode (field polarization azimuth $\theta = 90°$) [*Bahr*, 1988].

$$\begin{aligned} e_x &= M_{xx}\hat{\boldsymbol{x}} + M_{yx}\hat{\boldsymbol{y}} \\ e_y &= M_{xy}\hat{\boldsymbol{x}} + M_{yy}\hat{\boldsymbol{y}} \end{aligned} \tag{2}$$

where $\hat{\boldsymbol{x}}$ and $\hat{\boldsymbol{y}}$ are the unit vectors in the geographic north and east directions, respectively. In the 1-D case, the elements M_{xx} and M_{yy} are zero. In the 3-D case, the MT tensors are fully populated and generally asymmetric. Therefore, the electric field components (equation (1)) and the telluric components (equation (2)) associated with M_{xx} and M_{yy} are designated the anomalous components and M_{xy} and M_{yx} the regional components in this context.

The vertical magnetic field transfer functions (T_{zx}, T_{zy}, VTFs) give the linear relationship between vertical magnetic component B_z and horizontal components B_x and B_y in the frequency domain [*Simpson and Bahr*, 2005, p. 32] by

$$B_z = T_{zx}B_x + T_{zy}B_y \tag{3}$$

VTFs are often represented as complex induction vectors (or induction arrows)

$$T_z = T_{zx}\hat{\boldsymbol{x}} + T_{zy}\hat{\boldsymbol{y}} \tag{4}$$

Following the convention of *Parkinson* [1959], the real parts of the reversed induction arrows tend to point toward areas where electrical currents are concentrated. VTFs are in the range of 0 to 1 in general.

2.2. A 3-D Electrical Conductivity Model

The AWAGS data [*Chamalaun and Barton*, 1990] observed three-component magnetic time series simultaneously at 57 sites across Australia during 1989–1990, with an average spacing of 275 km between sites. *Wang et al.* [2014] inverted the VTFs (equation (3)) from the AWAGS data at periods of 360 s (6 min) to 9480 s (158 min) to derive a 3-D electrical conductivity model from a depth of 10 km to 600 km. The model has been compared with models inverted from MT data [*Thiel and Heinson*, 2013; *Duan et al.*, 2013] and shows good agreement in regional structures among the models inverted from VTFs and MT data [*Wang et al.*, 2014].

The model of *Wang et al.* [2014] consists of 21 horizontal layers to a depth of 648 km. The top five layers have thicknesses that vary progressively from 0.5 km to 1.5 km to a depth of 4.5 km. The known sedimentary basins and oceans are embedded in these shallow layers. The underlying 16 layers vary progressively in thickness from 2.5 km to 80 km. Horizontally, the model comprises a grid of 86×71 cells, with each cell being 55×55 km (approximately 0.5°), surrounded on all sides by a border of two 110×110 km (approximately 1°) cells, giving a total grid of 90×75 cells. The model is bounded by longitudes 110.0°E and 157.0°E and latitudes 7.0°S and 46.5°S.

In the 3-D numerical modeling using WSINV3DMT [*Siripunvaraporn and Egbert*, 2009], a plane wave source is located at the top of the model; electric fields and magnetic fields at the model surface sites are computed when the source field is in a northerly polarization mode and an easterly polarization mode respectively.

The electric fields E and magnetic fields B are calculated at 83 surface locations in total. Fifty-seven of these coincided with the AWAGS stations, and further, 26 were chosen to infill gaps to create an average station spacing of ~250 km. At each location the electric fields E and magnetic fields B are calculated for seven periods from 360 s to 9480 s. By using equation (1), the MT tensors are calculated, and then the telluric vectors are constructed by using equation (2). The telluric vectors at periods of 360 s (6 min) and 1800 s (30 min) are used to discuss the induction responses as these two periods are in the range relevant to GIC studies (i.e., a few seconds to approximately 30 min) [*Pulkkinen*, 2003; *Thomson et al.*, 2005].

3. Undistorted Induced Electric Field From a 1-D Model

The undistorted induced electric field from a 1-D model of the Earth is useful to understand the period dependence of geomagnetic induction and to serve as a reference for a complex 3-D model. A 1-D model may consist of either a homogenous half-space or N layers of different conductivities. In the following analysis, typical electrical conductivity values of Earth materials, which may range over many orders of magnitude, are used to consider both cases. The 1-D half-space model considered here is based on previous MT results from Australia, as used in the thin-sheet model of *Wang and Lilley* [1999], and uses an electrical conductivity of $\sigma = 10^{-3}$ S/m, and a simple two-layer model is constructed with the first layer of 10^{-3} S/m (σ_1) to a depth of 250 km (h_1) and then 10^{-1} S/m (σ_2).

The analytical solution of the electric field normalized by the magnetic field on the surface for plane wave source fields in two-layer model is [*Simpson and Bahr*, 2005, p. 24]

$$\frac{E_x(0)}{B_y(0)} = \frac{i\omega}{k_1} \cdot \frac{\frac{k_1}{k_2} + \tanh(k_1 h_1)}{1 + \frac{k_1}{k_2} \cdot \tanh(k_1 h_1)} \tag{5}$$

where $k_n = \sqrt{i\mu_0 \sigma_n \omega}$ and $n = 1, 2$. In the half-space case, $h_1 = 0$.

The induced electric fields for both models over a period range of 1 s to 10,000 s are computed using equation (5) for geomagnetic field variation having 1 nT amplitude. A simple example of the period dependence of

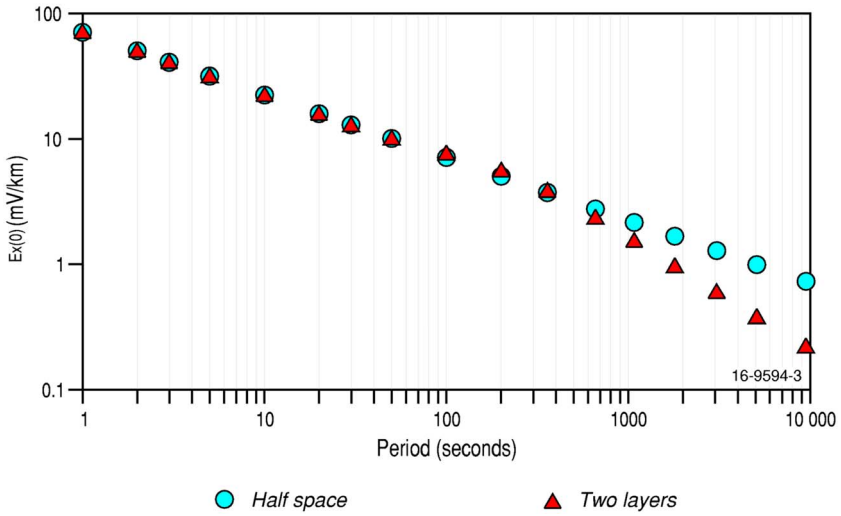

Figure 1. Magnitude of the induced electric fields in mV/km for $|B| = 1$ nT at the surface of Earth for half-space and two-layer models.

geomagnetic induction is shown in Figure 1 in which the magnitude of the induced electric field varies (decreases) as the period of the inducing magnetic field varies (increases).

Figure 1 also shows the effect of skin depth. At short periods (<50 s), the induced electric fields in both the half-space and two-layer model are the same because the skin depth of the short-period source field variations is much less than the thickness of the first layer of the two-layer model (e.g., the skin depth of a 50 s variation in a 10^{-3} S/m layer is about 110 km). The two-layer model is like a half-space for the short-period signals. At longer periods (>100 s), the induced electric fields of the half-space and two-layer models diverge in the log-log plot. This divergence is a direct consequence of the skin depth relationship: longer periods tend to penetrate deeper into the Earth, so the second layer of conductivity 10^{-1} S/m effectively influences the induced electric field in the two-layer model.

At periods of 360 s and 1800 s, the magnitudes of the electric fields induced in the two-layer model are 3.8 mV/km and 0.96 mV/km for $|B| = 1$ nT, respectively. These values will serve as reference values for the following 3-D models.

4. Distortions Arising From the Oceans

The influence of seawater plays a significant role in electromagnetic induction studies in the Australian region. Australia is an island continent surrounded by deep Indian Ocean to the west, Southern Ocean to the south, and Pacific Ocean to the east with shallow seas to the north. Three-component magnetometers operating individually, in pairs, and in linear and 2-D arrays, have been used in Australia to study anomalous geoelectrical structures since the pioneering work of *Parkinson* [1959]. One aspect of these magnetic induction studies was to investigate the deep oceans "coast effect" influence on the observed electric and magnetic fields on land [e.g., *Milligan*, 1988; *Ferguson et al.*, 1990; *Hitchman et al.*, 2000]. At stations near the coast, the induction arrow direction at the seven periods in Figure 2 clearly reflects the strong continent-ocean conductivity contrast nearby. The arrow length tends to vary at coastal stations, reflecting to some degree the distance to deep oceans, particularly to the north. At inland stations on cratons the induction arrows are of negligible length and arbitrary direction, and on stations near enhanced conductivity anomalies the induction arrows increase in length and clearly point toward the enhanced conductivity anomalies.

First, we consider features of coastal enhancement of a 21-layer simple 3-D ocean-continent (OC) model with the model space dimensions as defined in section 2.2. In the OC model, cells in the first five horizontal layers represent either continent ($\sigma = 10^{-3}$ S/m) or ocean ($\sigma = 3.33$ S/m). The underlying 16 1-D layers are assigned conductivities of 10^{-3} S/m to a depth of 250 km and then 10^{-1} S/m to 648 km. The OC model includes detailed bathymetry data for the seas [*Whiteway*, 2009].

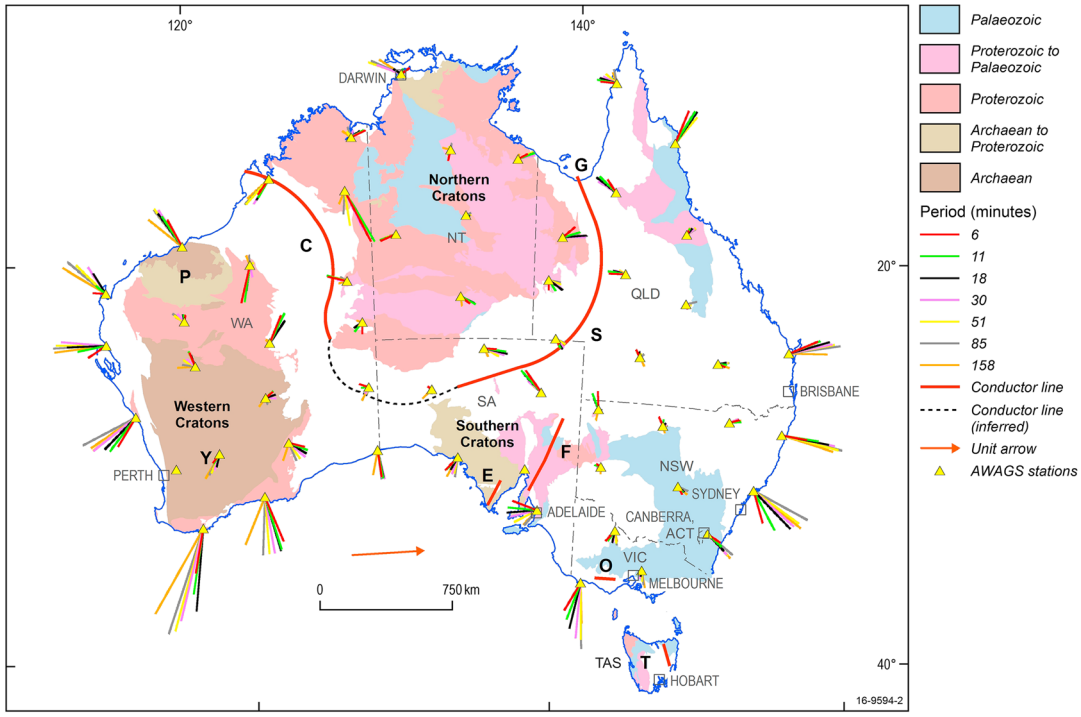

Figure 2. Australian geological setting broadly grouped into western, northern, and southern cratons. The solid red lines represent crustal-scale conductivity anomalies identified from magnetometer array studies—C: Canning Basin; S: Southwest Queensland; G: Carpentaria; E: Eyre Peninsula; F: Flinders; O: Otway; and T: Tamar—and the dashed line denotes possible continuity between anomalies proposed by *Chamalaun and Barton* [1993]. P: Pilbara Craton and Y: Yilgarn Craton in Western Australia. The yellow triangles show locations of AWAGS stations used in this study. The real parts of AWAGS vertical transfer functions (VTFs) are plotted as induction arrows at seven periods at each station [*Chamalaun and Barton*, 1993, Figure 6]. The red arrow to the south of the continent represents an induction arrow with length of 1, for scale.

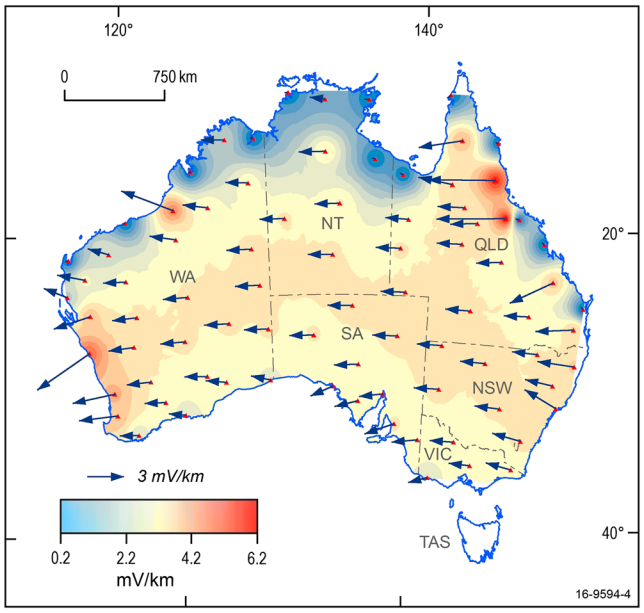

Figure 3. Magnitude of regional electric field component (E_y associated with M_{yx}) and telluric vectors of real e_x for a northerly polarization mode derived from the OC model for $|B| = 1$ nT at a period of 360 s.

Figures 3 and 4 show the magnitude of the regional component of the induced electric fields (shown by the colored background on the maps) and the real part of telluric vectors (shown by the arrows) in both polarization modes for the OC model for $|B| = 1$ nT at a period of 360 s. In the center of the continent, the electric field magnitude for the OC model at 360 s is around 3.5 mV/km, slightly less than the 3.8 mV/km previously determined for the undisturbed background. This difference reflects the differing features of the simple two-layer model and the OC 3-D model which incorporates oceans and coastline geometry. The value of 3.5 mV/km is taken as background regional value for a northerly polarization mode and an easterly polarization mode in the OC model in the inland area.

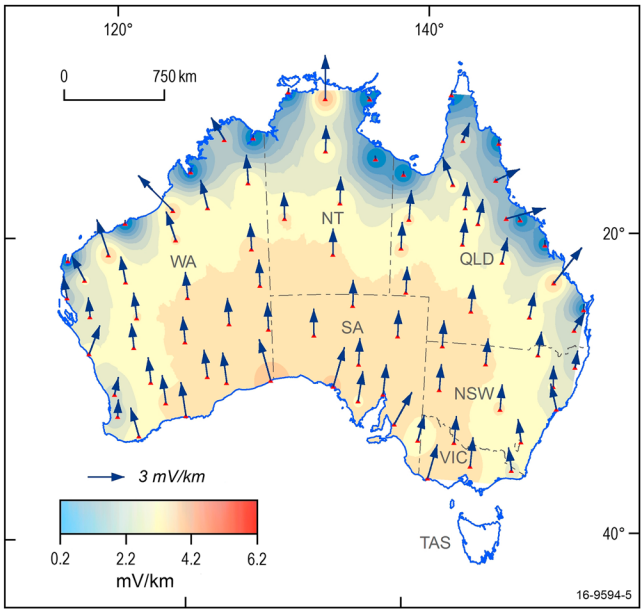

Figure 4. Magnitude of regional electric field component (E_x associated with M_{xy}) and telluric vectors of real e_y for an easterly polarization mode derived from the OC model for $|B| = 1$ nT at a period of 360 s.

Distortions in the magnitude of the regional electric field components occur in all the coastal areas. In general, the N-S striking coastlines on the east and west coasts have very narrow continental shelf margins, dropping steeply to the deeper ocean. This results in a sharp lateral variation of conductivity across the ocean-land boundary. A northerly polarization mode (Figure 3) induces mainly E-W current flow which is approximately perpendicular to the N-S striking coastlines. In order to maintain continuity of the normal component of current density across the ocean-land boundary, a large electric field occurs in the vicinity of the approximately N-S striking coastline. The electric field reduces in the same area for an easterly polarization mode as the current flow is almost parallel to the coastlines.

For an easterly polarization mode (Figure 4), distortion in the induced electric field mainly occurs in the northern and southern coastal areas where E-W striking coastlines show enhancement in the electric field, for example, the southern coastline of the Great Australian Bight south of latitude −30° (Figure 4) where there is a narrow continental shelf margin.

The telluric vectors (equation (2)) for both polarization modes clearly show angular distortion of the induced electric field due to coasts. For example, in the northeast of the continent on the Queensland coast, the northerly polarization mode (Figure 3) telluric vectors tend to increase in length but remain almost parallel when compared with telluric vectors in central Australia. For the easterly polarization mode (Figure 4), angular distortions of telluric vectors tend to be large with the telluric vector diverging approximately 60° from north. This suggests that angular distortion in the electric field may be sensitive to the polarization mode of the source field and the orientation of the coastline.

The anomalous electric field components (associated with M_{xx} and M_{yy}) present clearer evidence of electric field enhancement due to the lateral contrast between ocean and land (Figure 5). In general, the anomalous component tends to be zero away from the coast where electrical conductivity structure is close to 1-D and gradually increases to 2.8 mV/km or decreases to −2.8 mV/km toward the coast. For a northerly polarization mode, the NW-SE striking coastal area has a negative anomalous component, while the NE-SW striking coastal area has a positive anomalous component. Similar to the northerly polarization mode, the enhancement in electric field in the coast area is also present in the easterly polarization mode.

5. Distortions Arising From 3-D Conductivity Structures

The 3-D model in Figure 6 reflects broad electrical conductivity structures beneath the continent. Key features of the model include major enhanced conductivity anomalies in Archaean cratonic areas in Western Australia and Phanerozoic terrains to the east of the continent and an enhanced conductivity structure at middle-lithosphere depths across much of central Australia [*Wang et al*., 2014].

The spatial distributions of the electric field are affected significantly by onshore electrical conductivity structures when compared to the OC model considered in section 4. In general, the electric field and telluric vectors are enhanced in the more resistive regions of the continent and are suppressed in the conductive regions as shown in Figure 6. Key features are discussed below.

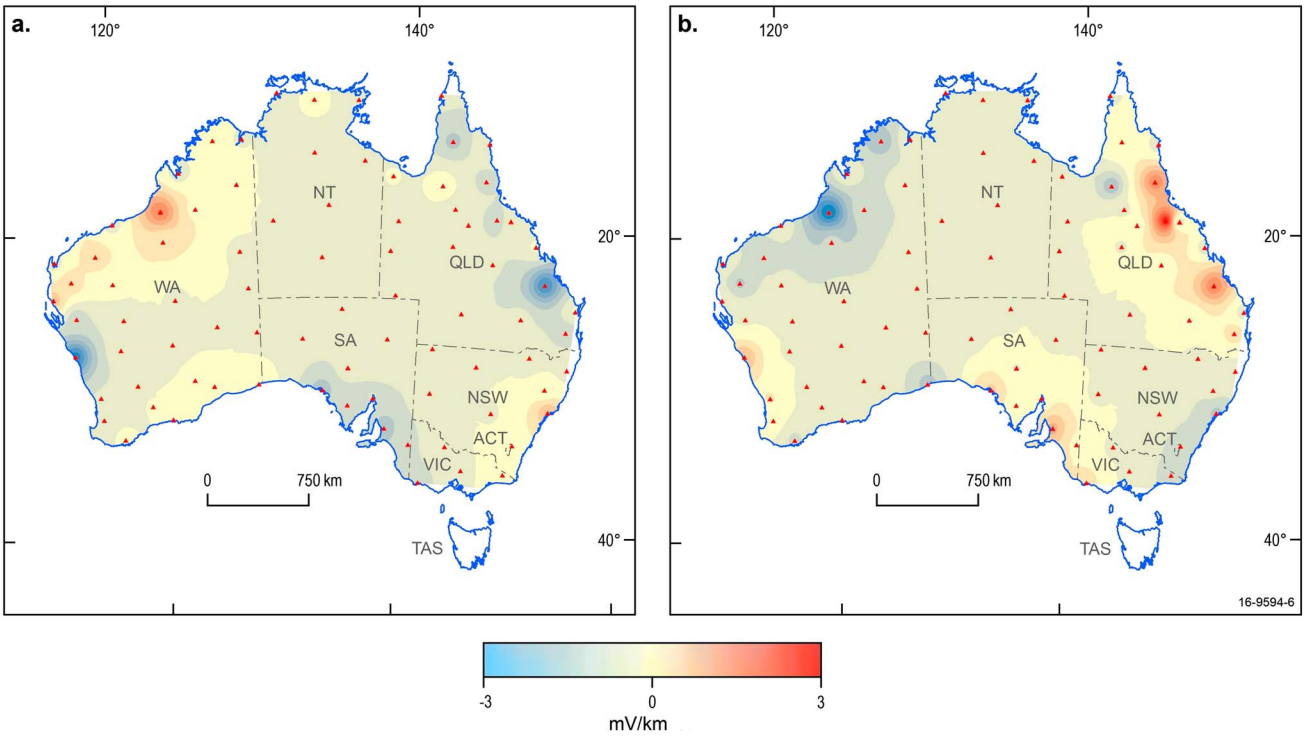

Figure 5. (a) Real part of anomalous electric field component (E_x associated with M_{xx}) in a northerly polarization mode. (b) Real part of anomalous electric field component (E_y associated with M_{yy}) in an easterly polarization mode for $|B| = 1$ nT at a period of 360 s.

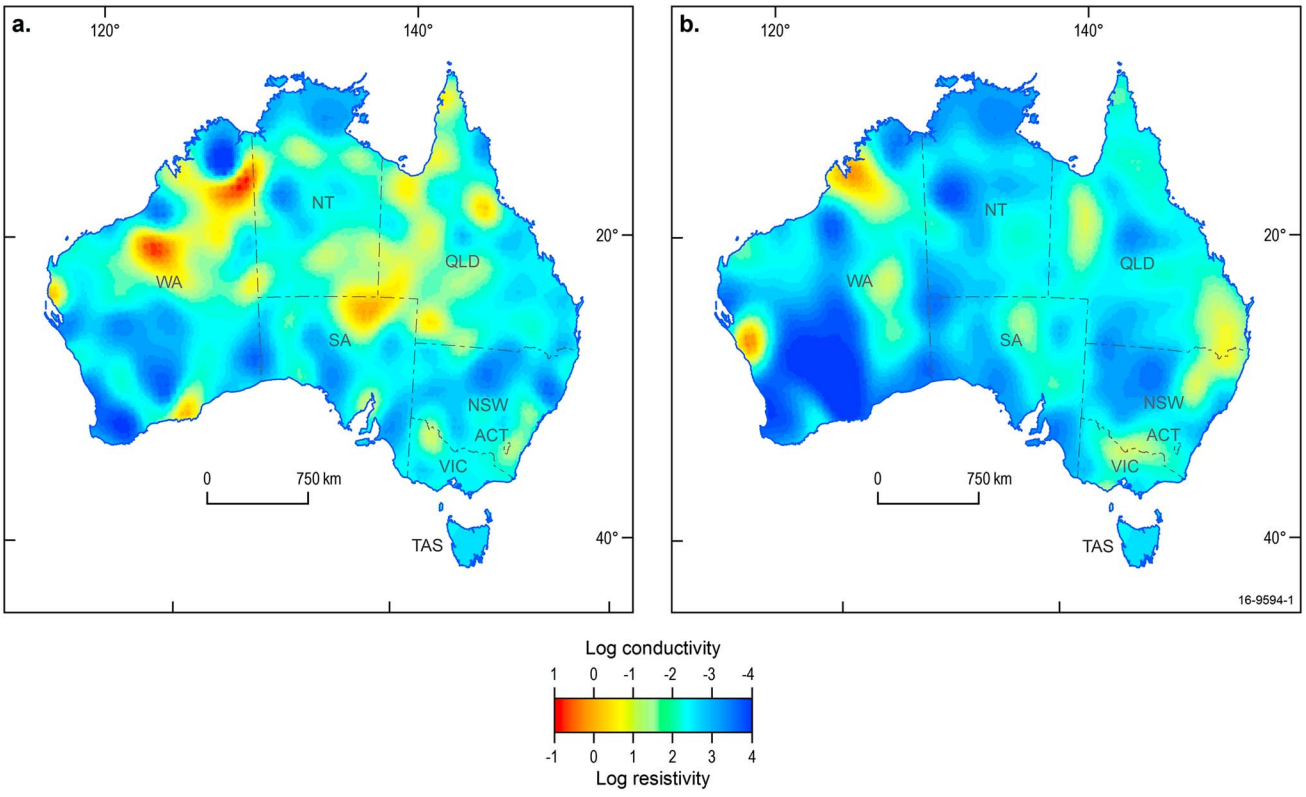

Figure 6. The 3-D electrical conductivity model of the Australian region with conductivity images at depths of 25 km and 170 km. Adapted from Figure 7 of *Wang et al.* [2014].

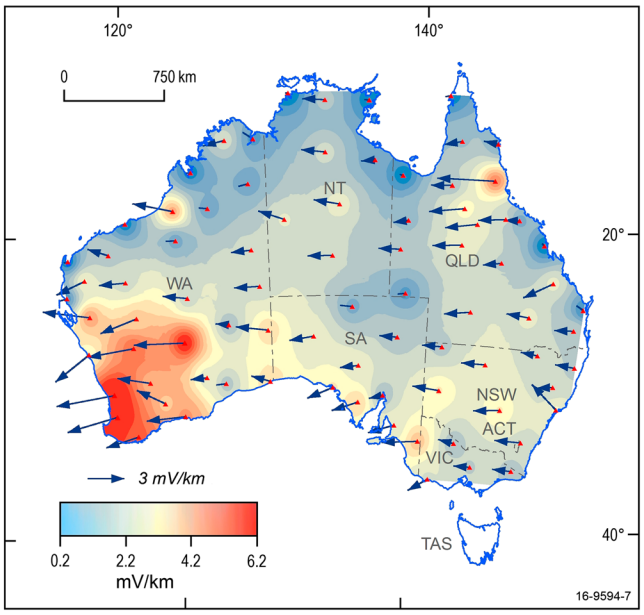

Figure 7. Magnitude of regional electric field component (E_y associated with M_{yx}) and telluric vectors of real e_x for a northerly polarization mode for $|B| = 1$ nT at a period of 360 s.

5.1. Enhanced Electric Field in Western Australia

The Western Australian (WA) landmass consists of the Archaean Yilgarn Craton (Y, Figure 2) to the south and Pilbara Craton (P, Figure 2) to the north, joined along the Capricorn Orogen [*Myers et al.*, 1996]. The 3-D model (Figure 6) shows that the Yilgarn Craton is well defined by conductivity values less than 10^{-3} S/m at crustal depths, continuing to depths beyond 250 km. Pilbara Craton conductivity values are a few 10^{-1} S/m, continuing to below 100 km [*Wang et al.*, 2014].

Once these two conductivity structures are incorporated in the modeling, the induced electric field on the resistive Yilgarn Craton is increased in comparison with the conductive region in the east of the model. The length of the telluric vectors is increased by a factor of up to 2 with respect to the 3.5 mV/km of the OC model (compare Figures 7 and 8 with Figures 3 and 4), and the enhanced electric field persists inland for approximately 1000 km. Toward the conductive Pilbara Craton in the north, the induced electric field is reduced by a factor of 2 to 3 times the values on the resistive Yilgarn Craton and is substantially different from the response of the OC model.

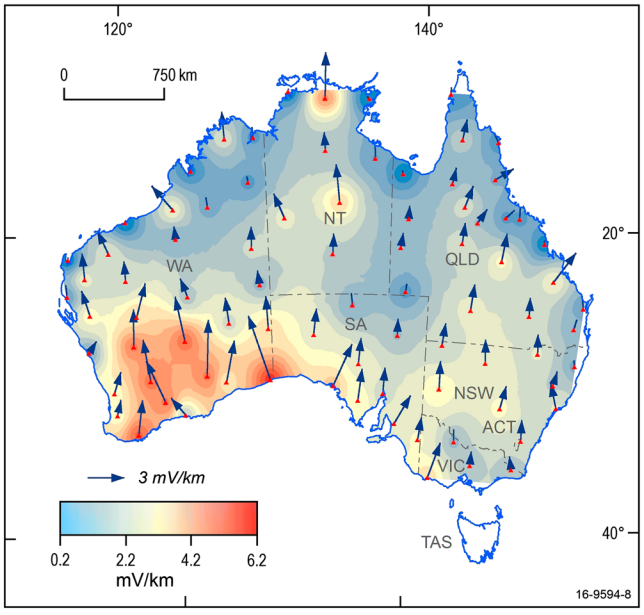

Figure 8. Magnitude of regional electric field component (E_x associated with M_{xy}) and telluric vectors of real e_y for an easterly polarization mode for $|B| = 1$ nT at a period of 360 s.

A few regions of localized enhanced electric fields in Figures 7 and 8 correspond to isolated resistive structures in Figure 6 which are mainly due to the coarse 55 km grid size of the data mesh used in the 3-D model.

5.2. Reduced Electric Field in the Area of the High-Conductivity Anomalies

The major crustal high-conductivity anomalies in continental Australia are the Carpentaria (G, Figure 2) and Southwest Queensland (S, Figure 2) anomalies. The Carpentaria anomaly in Queensland is represented as a highly conducting zone in the crust extending down tens of kilometers to penetrate the mantle [*Lilley et al.*, 2003]. The Southwest Queensland anomaly, originally mapped by *Woods and Lilley* [1980], is at crustal depths. The 3-D model of *Wang et al.* [2014] suggests that both high-conductivity structures form a major

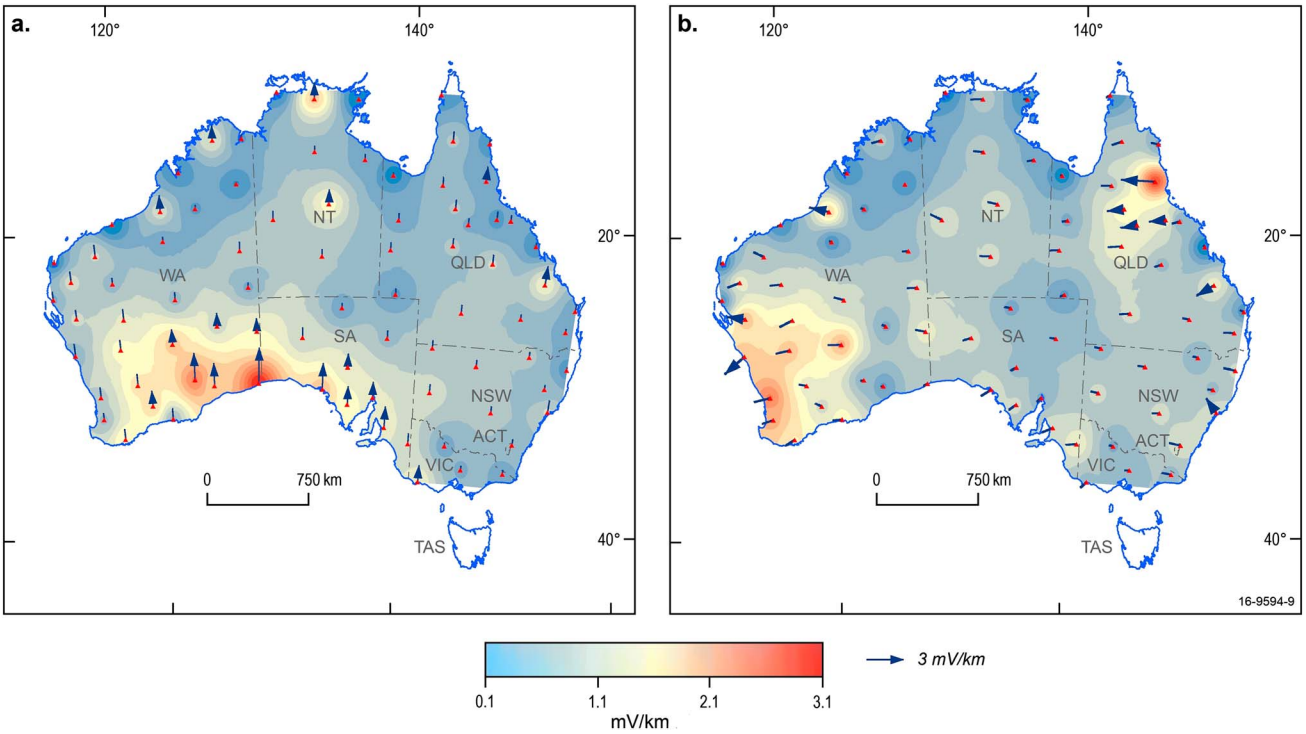

Figure 9. (a) Magnitude of regional electric field component E_x (associated with M_{xy}) and telluric vectors of real e_y for an easterly polarization mode at a period of 1800 s. (b) Magnitude of regional electric field component E_y (associated with M_{yx}) and telluric vectors of real e_x for a northerly polarization mode at a period of 1800 s.

conductivity anomaly extending to a depth of about 100 km. Figures 7 and 8 show that the electric field magnitude tends to reduce to approximately 1 mV/km in the area of these high-conductivity anomalies. This highlights the significant distorting effect of inland conductivity anomalies on the electric field with respect to the OC model.

In coastal areas between latitudes −20° and −10° the inverted enhanced conductivity structures on land cause smooth variation across the ocean-land boundary. This effectively reduces the conductivity contrast between ocean and land, which in turn reduces the amplitude of the electric field on the land side with respect to the OC model. For example, the Cape York Peninsula and the Gulf of Carpentaria area in North Queensland were imaged with a conductivity of a few tenths of S/m, in contrast to 10^{-3} S/m in southern coastal areas south of latitude −30° (Figure 6). This phenomenon is also evident in the observed VTFs data in Figure 2 where the induction arrows show that the coast effect is significantly smaller in coastal areas north of latitude −20° compared to that seen in coastal areas south of latitude −20°.

5.3. Less Distorted Electric Field in Central and Southeast Australia

At a period of 360 s, the source field has a skin depth of about 30 km in sedimentary basins with a conductivity of 10^{-1} S/m; therefore, the model at a depth of 25 km shown in Figure 6 will have greater influence on the electric field at the surface. At a depth of 25 km, the majority of central and eastern Australia has structures of moderate-to-low conductivity (10^{-2} S/m to 10^{-3} S/m) with smooth variations of electrical structures across the regions. The magnitude of the regional component is approximately 3.0 mV/km, which is close to the OC model background value of 3.5 mV/km.

5.4. Influence of Deeper Conductivity Structures at a Longer Period

When the period of the source field is increased to 1800 s, the penetration depth of the source field increases and in turn deeper electrical conductivity structures (Figure 6b) influence the electric field at the surface. Distortion in the electric field (Figure 9) shows less variation inland compared to Figures 7 and 8. For

reference, the amplitude of the electric field at the surface is approximately 0.96 mV/km at a period of 1800 s for the undisturbed background (Figure 1). Figure 9 also shows that distortions in the electric field have similar features compared with Figures 7 and 8. For example, the Archaean Yilgarn Craton and south coast of Western Australia have greater enhanced electric field, and distortion in the east and west coasts is prominent.

6. Implications and Conclusions

We have discussed the electric field distribution in the Australian region at a period of 360 s for both a simple 3-D ocean-continent (OC) model and a more detailed 3-D conductivity model. In general, the regions south of latitude −20° are exposed to more induction hazards than northern Australia. On the northern coast the enhanced electrical conductivity structures reduce the conductivity contrast between coast and ocean thus reducing the electric field. The electric field is significantly increased on the resistive Western Australia craton but reduced in central Australia where enhanced electrical conductivity anomalies exist.

The simplified 3-D OC model accounts for some of the electric field due to the oceans but has been shown to be inadequate on land areas and on coastlines where complex resistivity structures exist. The Australian continent requires a detailed 3-D model to more accurately characterize the electrical conductivity structures for geomagnetic induction hazard studies.

In Australia, Geoscience Australia and the Bureau of Meteorology operate observatory and variometer station networks that continuously monitor magnetic field activity. *Marshall et al*. [2010] developed an algorithm for GIC estimation from magnetic fields and simple 1-D depth-dependent electrical conductivity models. Our study, made using MT tensors derived from 3-D modeling of an electrical conductivity model, shows that the estimation method based on 1-D assumptions may be valid in central and southeast Australia where electric fields are less distorted (section 5.3) but will lead to inaccurate GIC estimates in Western Australia, the inland areas where high-conductivity anomalies exist, and coastal areas. Estimation of the induced electric fields across the Earth's surface requires detailed modeling of the 3-D lithospheric conductivity [*Love and Swidinsky*, 2015].

Our method used the MT tensors calculated from a 3-D electrical conductivity model inverted from the VTFs data, which has a broad spatial resolution to 3-D Earth conductivity. *Bedrosian and Love* [2015] used empirical impedance tensors directly from field measurements, which has detailed resolution. Both approaches are complementary to each other and have demonstrated improvements in GIC estimates over those calculated from simple 1-D depth-dependent electrical conductivity models. Geoscience Australia is currently participating in possibly the largest MT program in the world, the Australian Lithospheric Architecture Magnetotelluric Program (AusLAMP) [*Stolz*, 2013]. Long-period MT data will be collected at approximate 2800 stations on a 50 by 50 km grid spacing covering the whole of the Australian continent. So far, data have been acquired at about 500 of these AusLAMP stations. A detailed 3-D electrical conductivity model will inevitably follow from these data which will benefit the study of GIC in Australia.

Acknowledgments

The authors thank Adrian Hitchman and Murray Richardson for reviewing a draft manuscript. Numerical calculations were carried out on TSUBAME 2.0 at the Global Scientific Information and Computing Center of the Tokyo Institute of Technology. The AWAGS data and the 3-D electrical conductivity model derived from the AWAGS data are available upon request (geomag@ga.gov.au). The AWAGS data are archived at the Geomagnetism group, Geoscience Australia. We thank Editor Delores Knipp, Associate Editor, and two anonymous reviewers for their valuable reviews which have significantly improved this paper. This paper is published with the permission of the CEO, Geoscience Australia.

References

Bahr, K. (1988), Interpretation of the magnetotelluric impedance tensor: Regional induction and local telluric distortion, *J. Geophys.*, *62*, 119–127.

Barton, C. E. (1997), An "aeromagnetic risk map" of Australia, in *Transient and Induced Variations in Aeromagnetics*, edited by P. R. Milligan and C. E. Barton, Austral. Geol. Surv. Org., Record, 1997/27, 27–29.

Bedrosian, P. A., and J. J. Love (2015), Mapping geoelectric fields during magnetic storms: Synthetic analysis of empirical United States impedances, *Geophys. Res. Lett.*, *42*, 10,160–10,170, doi:10.1002/2015GL066636.

Boteler, D. H., R. J. Pirjola, and H. Nevanlinna (1998), The effects of geomagnetic disturbances on electrical systems at the Earth's surface, *Adv. Space Res.*, *22*, 17–27, doi:10.1016/S0273-1177(97)01096-X.

Campbell, W. H., and E. R. Schiffmacher (1988), Quiet ionospheric currents of the southern hemisphere derived from geomagnetic records, *J. Geophys. Res.*, *93*, 933–944, doi:10.1029/JA093iA02p00933.

Chamalaun, F. H., and C. E. Barton (1990), Comprehensive mapping of Australia's geomagnetic variations, *EOS, Trans. AGU*, *71*(1867), 1873.

Chamalaun, F. H., and C. E. Barton (1993), Electromagnetic induction in the Australian crust: Results from the Australia-wide Array of Geomagnetic Stations, *Explor. Geophys.*, *24*, 179–186.

Duan, J., P. R. Milligan, and T. Fomin (2013), Electrical resistivity distribution from magnetotelluric data in the Yilgarn Craton, western Officer Basin and western Musgrave Province, in *Yilgarn Craton-Officer Basin-Musgrave Province Seismic and MT Workshop*, edited by N. L. Neumann, pp. 9–23, Geoscience Australia, Record, 2013/28.

Ferguson, I. J., F. E. M. Lilley, and J. H. Filloux (1990), Geomagnetic induction in the Tasman Sea and electrical conductivity structure beneath the Tasman Seafloor, *Geophys. J. Int.*, *102*, 299–312.
Fernberg, P. A., C. Samson, D. H. Boteler, L. Trichtchenko, and P. Larocca (2007), Earth conductivity structures and their effects on geomagnetic induction in pipelines, *Ann. Geophys.*, *25*, 207–218.
Hitchman, A. P., F. E. M. Lilley, P. R. Milligan, A. White, and G. S. Heinson (2000), The total-field geomagnetic coast effect: The CICADA97 line from deep Tasman Sea to inland NSW, *Explor. Geophys.*, *31*, 52–57.
Lilley, F. E. M., A. P. Hitchman, and L. J. Wang (1999), Time-varying effects in magnetic mapping: Amphidromes, doldrums, and induction hazard, *Geophysics*, *54*(6), 1720–1729.
Lilley, F. E. M., L. J. Wang, F. H. Chamalaun, and I. J. Ferguson (2003), Carpentaria electrical conductivity anomaly, Queensland, as a major structure in the Australian Plate, in *Evolution and Dynamics of the Australian Plate*, *Geological Society of Australia Special Publication 22 and Geological Society of America Special Paper 372*, edited by R. R. Hillis and R. D. Muller, pp. 141–156, Geol. Soc. Am., Boulder, Colo.
Love, J. J., and A. Swidinsky (2015), Observatory geoelectric fields induced in a two-layer lithosphere during magnetic storms, *Earth Planets Space*, *67*, 58, doi:10.1186/s40623-015-0213-3.
Marshall, R. A., C. L. Waters, and M. D. Sciffer (2010), Spectral analysis of pipe-to-soil potentials with variations of the Earth's magnetic field in the Australian region, *Space Weather*, *8*, S05002, doi:10.1029/2009SW000553.
Marshall, R. A., E. A. Smith, M. J. Francis, C. L. Waters, and M. D. Sciffer (2011), A preliminary risk assessment of the Australian region power network to space weather, *Space Weather*, *9*, S10004, doi:10.1029/2011SW000685.
Marshall, R. A., M. Dalzell, C. L. Waters, P. Goldthorpe, and E. A. Smith (2012), Geomagnetically induced currents in the New Zealand power network, *Space Weather*, *10*, S08003, doi:10.1029/2012SW000806.
Milligan, P. R. (1988), Short-period transfer function vectors for Canberra and Charters Towers magnetic observatories, *J. Geomag. Geoelectr.*, *40*, 95–103.
Myers, J. S., R. D. Shaw, and I. M. Tyler (1996), Tectonic evolution of Proterozoic Australia, *Tectonics*, *15*, 1431–1446, doi:10.1029/96TC02356.
Parkinson, W. D. (1959), Direction of rapid geomagnetic fluctuations, *Geophys. J. R. Astron. Soc.*, *2*, 1–14.
Parkinson, W. D. (1962), The influence of continents and oceans on geomagnetic variations, *Geophys. J. R. Astron. Soc.*, *4*, 441–449.
Pulkkinen, A. (2003), Geomagnetic induction during highly disturbed space weather conditions: Studies of ground effects, PhD thesis, Dep. Of Physical Sciences, Univ. of Helsinki, Finland.
Simpson, F., and K. Bahr (2005), *Practical Magnetotellurics*, Cambridge Univ. Press, Cambridge.
Siripunvaraporn, W., and G. Egbert (2009), WSINV3DMT: Vertical magnetic field transfer function inversion and parallel implementation, *Phys. Earth Planet. Inter.*, *173*, 317–329.
Stolz, N. (2013), New national magnetotelluric survey gets underway, AusGeo News, 112, Geoscience Australia.
Thiel, S., and G. Heinson (2013), Electrical conductors in Archaean mantle—Result of plume interaction?, *Geophys. Res. Lett.*, *40*, 2947–2952, doi:10.1002/grl.50486.
Thomson, A. W. P., A. J. McKay, E. Clarke, and S. J. Reay (2005), Surface electric fields and geomagnetically induced currents in the Scottish Power grid during the 30 October 2003 geomagnetic storm, *Space Weather*, *3*, S11002, doi:10.1029/2005SW000156.
Wang, L. J., and F. E. M. Lilley (1999), Inversion of magnetometer array data by thin-sheet modelling, *Geophys. J. Int.*, *137*, 128–138.
Wang, L. J., A. P. Hitchman, Y. Ogawa, W. Siripunvaraporn, M. Ichiki, and K. Fuji-ta (2014), A 3-D conductivity model of the Australian continent using observatory and magnetometer array data, *Geophys. J. Int.*, *198*(2), 1171–1186, doi:10.1093/gji/ggu188.
Weaver, J. T., A. K. Agarwal, and F. E. M. Lilley (2000), Characterization of the magnetotelluric tensor in terms of its invariants, *Geophys. J. Int.*, *141*, 321–336.
Whiteway, T. G. (2009), Australian bathymetry and topography grid, June 2009, 46 pp., Geoscience Australia, Record, 2009/21.
Woods, D. V., and F. E. M. Lilley (1980), Anomalous geomagnetic variations and the concentration of telluric currents in southwest Queensland, Australia, *Geophys. J. R. Astron. Soc.*, *62*, 675–689.
Zhang, J. J., C. Wang, T. R. Sun, C. M. Liu, and K. R. Wang (2015), GIC due to storm sudden commencement in low-latitude high-voltage power network in China: Observation and simulation, *Space Weather*, *13*, 643–655, doi:10.1002/2015SW001263.